Journal of Materials Science & Technology 105 (2022) 36–44

Contents lists available at ScienceDirect

Journal of Materials Science & Technology

journal homepage: www.elsevier.com/locate/jmst

Phase orientation improved the corrosion resistance and conductivity of Cr_2AlC coatings for metal bipolar plates

Guanshui Ma[a], Dong Zhang[a], Peng Guo[a], Hao Li[a,b], Yang Xin[a], Zhenyu Wang[a], Aiying Wang[a,b,c,*]

[a] Key Laboratory of Marine Materials and Related Technologies, Zhejiang Key Laboratory of Marine Materials and Protective Technologies, Ningbo Institute of Materials Technology and Engineering, Chinese Academy of Sciences, Ningbo 315201, China
[b] Center of Materials Science and Optoelectronics Engineering, University of Chinese Academy of Sciences, Beijing 100049, China
[c] Ningbo Institute of Industrial Technology,Ningbo 315201, China

ARTICLE INFO

Article history:
Received 8 March 2021
Revised 3 June 2021
Accepted 12 June 2021
Available online 12 September 2021

Keywords:
$M_{n+1}AX_n$ phase coating
Metal bipolar plate
Interface contact resistance
Corrosion resistance

ABSTRACT

In view of the $M_{n+1}AX_n$ (MAX) phase coatings benefiting the adaptive passivation film for good corrosion resistance and high electronic density of states for excellent electrical conductivity, here, we reported the Cr_2AlC MAX phase coatings with different preferred orientations by a homemade technique consisting of vacuum arc and magnetron sputtering. The dependence of surface and interface microstructural evolution upon the corrosion and electrochemical properties of deposited coating was focused. Results showed that all the Cr_2AlC coatings with different phase orientations greatly improved the performance of stainless steel (SS) 316 L substrate. Specifically, the lowest value of interface contact resistance (ICR) reached to 3.16 mΩ cm^2 and the lowest corrosion current density was 2×10^{-2} μA cm^{-2}, which were much better than those of bare SS316L. The combined studies of electrochemical properties and theoretical calculations demonstrated that the Cr_2AlC coatings with preferred (103) orientation were easier to form oxide passivation film on their surface to increase the corrosion resistance.

1. Introduction

With increasing demands of eco-environment and eco-energy in the world, fuel cells have been considered as one strong candidates of green energy for many industrial applications, particularly in electrical transportation application fields [1]. In particular, different with the solid oxide fuel cells, proton exchange membrane fuel cells (PEMFCs) attract the most spotlight due to their combined privileges of small size, lightweight, near-zero emission, fast startup and high efficiency of energy conversion [2,3]. Since 2004, the United States Department of Energy (US DOE) has spent an average of about $139 million per year on PEMFCs [4], and more than 5000 fuel cell vehicles and 20,000 forklifts powered by PEMFCs have been operated recently. In Japan, Toyota also commercialized the first PEMFCs vehicles in 2017, and it reached nearly 5000 vehicles at the middle of 2018 [5]. Very recently, the study on hydrogen-fueled PEMFCs for automobile applications has becoming more and more important than before in china to peak carbon dioxide emissions before 2030 and achieve carbon neutrality before 2060.

The bipolar plates (BPs), as a prime component and key part in PEMFCs stack manufacturing, accounting for about 45% of stack cost and at least 80% of weight, which serve as the important functions such as carrying current from cells, dislodging heat from the active areas, preventing leakage of reactants and coolant, and so on [6,7]. At present, many BPs materials are fabricated for PEMFCs including graphite, polymer composite and metallic BPs materials. The composite materials as a new type of candidate combine polymer materials and conductive fillers, owning the advantages of lightweight, small volume and good corrosion resistance. However, the excessive conductive fillers have to be added to increase the electrical conductivity, which leads to a decrease of mechanical properties [8]. Graphite is the most widely used material in bipolar plates industry, because of its intrinsic excellent electrical conductivity and corrosion resistance. But, the large cost of the graphite in manufacturing flow distribution pattern and light-reduction induced brittleness are becoming the main barriers to the widespread marketplace [9]. Compared to composite and graphite BPs, metallic BPs possess the high strength, excellent mechanical durability and good electrical conductivity, which makes

* Corresponding authors.
E-mail addresses: wangzy@nimte.ac.cn (Z. Wang), aywang@nimte.ac.cn (A. Wang).

https://doi.org/10.1016/j.jmst.2021.06.069
1005-0302/

them the combined priority of high performance, lightweight and space savings essential for transport applications [10]. Currently, several metals and metallic alloys, such as aluminum [11], titanium [12], stainless steel (SS) [6], copper alloys [13] and nickel alloys [14], have been attempted for the BPs component in PEMFCs. Among them, SS316L owns the most promising advantages as BPs substrate, because of its higher electrical conductivity, lower cost as well as better machinability, which benefits the facile fabrication of required shape to accommodate complex flow channels in PEMFCs [15]. However, the SS316L BPs are preferred to corrosion and dissolution when used in a typical humid, acidic and temperature around 80°C under the PEMFCs systems. The metal ions released from corrosion can lead to catalyst poisoning and the formed passive film will increase the interface contact resistance (ICR) of the electrode plates, which significantly deteriorate the output power and service life of the PEMEFCs system.

Recently, various types of coatings have been widely employed to modify the surface properties of BPs, such as noble metal coating [10,16], carbon-based coating [17], metal nitride coating [18] and metal carbide coating [19,20]. Wang et al. [21] and Northwood et al. [22] suggested that the property of SS BPs with gold coating was similar to that of graphite in simulated PEMFCs environments, but limited by the expensive cost of the gold coating. Alternatively, Yi et al. [23] demonstrated TiC_x/a-C nanolayered coating and Cr-N-C multilayer coatings on SS316L as BPs for PEMFCs, and the result showed that the corrosion resistance and electrical conductivity were significantly enhanced, which could meet the requirements of U.S DOE target. However, during the long-term service of PEMFCs, it still remains a great challenge to keep the coating with high corrosion resistance and low ICR, which greatly affects the stability and life of the battery system [5]. Therefore, it is urgent and important to exploit new protective coatings for metal BPs.

Different from the traditional transition metal nitrogen/carbide coating, $M_{n+1}AX_n$ phases (MAX phases) are a new class of materials that bridge the gap between metals and ceramics with close packed hexagonal structure [24-26]. Benefiting from their unique layered structure and bonding characteristics, MAX phases possess excellent oxidation resistance, outstanding electrical and thermal conductivities [27], which have been developed for corrosion resistance and conductivity applications in sulfuric acid and alkali solutions [28-30]. Zhu et al. [31,32] elaborated that Ti_3AlC_2 and Ti_3SiC_2 coatings exhibited an excellent ICR and good corrosion resistant performance. The ICR of the SS304 with Ti_3AlC_2 coating was 3.725 mΩ cm^2 and the lowest corrosion current densities value was as low as 4.4×10^{-7} A cm^{-2}. Li et al. [29] compared the corrosion resistance of Ti_3AlC_2 in 1 M H_2SO_4 and NaOH solutions. The results showed that Ti_3AlC_2 formed dense and stable TiO_2 passivation film in NaOH solution, while in H_2SO_4 solution it formed a sub-stoichiometricTiO_{2-x} metastable passivation film, which made its corrosion resistance worse than that of NaOH solution.

With regards to corrosion medium, in a general sense, the corrosion resistance is ascribed to the formation of protective film [33-36], which originates from the differences between the atomic packing densities of crystal orientation [37-43]. Ma et al. [44] put forward a surface step dissolution model in term of faster dissolution of the (111) closest packed planes and reported an defined relationship between grain orientations and the corrosion performance of 90Cu-10Ni alloy. Wen et al. [45] found that the orientation-dependent corrosion behavior of the nickel-based single crystal superalloys was mainly related to the compactness of the passive film, which based on the surface equivalent atomic packing density. Terryn et al. [46] reported that the passive layer formed on the<111>//ND orientation was thicker and more protective than that formed on the<001>//ND orientation for the passivated copper. Therefore, it could be said that the formed passive film played a key factor to elucidate the orientation-dependent corrosion mechanism.

In family of MAX phase compounds, Cr_2AlC has recently attracted considerable interest as a result of its excellent oxidation and corrosion resistance, as well as facile preparation with low phase-forming temperature. Meanwhile, Cr_2AlC exhibits the similar thermal expansion at 13.3×10^{-6} K^{-1} as that of SS316L at 17×10^{-6} K^{-1}, which not only benefits the good adhesion between substrate and coating, but also suppresses the possible cracking of coatings during the post-annealing process [47]. More importantly, the excellent electrical conductivity of $(1.4–2.3) \times 10^{-6}$ Ω^{-1} m^{-1} for Cr_2AlC yields the high-power privilege in harsh PEMFCs conditions [48].

In this study, the Cr_2AlC coatings with different crystal phase orientations at various thickness transition layers were successfully prepared by a combined arc/sputtering vacuum deposition system along with vacuum annealing. The ICRs and corrosion resistances of SS316L coated by Cr_2AlC MAX phase were focused in a simulated corrosive PEMFC environment, as well as the uncoated SS316L for comparison. The corrosion behavior was evaluated using electrochemical technique, and the passive films were confirmed by transmission electron microscopy (TEM) and X-ray photoelectron spectroscopy (XPS). Moreover, a corrosion mechanism that was dependent on the preferred orientation of Cr_2AlC coatings was discussed in terms of the density-functional theory (DFT) calculations and combined experimental results.

2. Experimental section

2.1. Cr_2AlC MAX phase coatings preparation

The synthesis procedures of Cr_2AlC MAX phase coating were shown in Fig. 1. Firstly, the Cr-C was deposited as transition layer on the SS316L substrate. Secondly, Cr-Al-C layer was deposited on the top of Cr-C layer. Finally, the SS316Ls with coatings were annealed under a vacuum condition, and then the top layer with Cr_2AlC MAX phase was obtained with Cr_3C_2 transition layer.

The Cr_2AlC coatings were fabricated on SS316L substrates by the arc combined sputtering method along with vacuum annealing. The composition of the used SS316L was listed in supporting information Table S1. All the SS316L substrates with a diameter of 15 mm were ground with No. 800–5000 grit by SiC abrasive papers, and polished sequentially by No. 5 diamond paste polisher. Before putting them into the chamber, the SS316L substrates were ultrasonically cleaned by acetone and alcohol for 20 min to remove residual surface contaminates, and dried using high-purity N_2. The aluminum target was applied as sputtering source and the chromium target was used as cathode arc source. All purity of targets was 99.9%. And CH_4 was used as reactive gas for carbon source. Before deposition, the chamber was heated to 200 °C, then the chamber vacuum was pumped to a low pressure of 3×10^{-5} Pa to eliminate air. To further clean the surface, all SS316L substrates were etched by Ar^+ ions for 30 min. The Cr-C transition layer was deposited with different time (20, 40, 60 min) at 70 A current, and the Cr-Al-C coating was deposited for 120 min by sputtering the Cr and Al targets with the applied power of 17 W and 3.0 kW, respectively. The obtained samples were named S20, S40 and S60, respectively. At the same time, the sample only with a single Cr-C layer deposited with 60 min or a single Cr-Al-C layer deposited with 120 min was also provided, the target current and power remained unchanged. After deposition, the annealing treatment for as-deposited coatings was applied at 440 °C for 96 h with 1.0×10^{-3} Pa vacuum. Supporting information Table S2 provided the details of the deposition conditions.

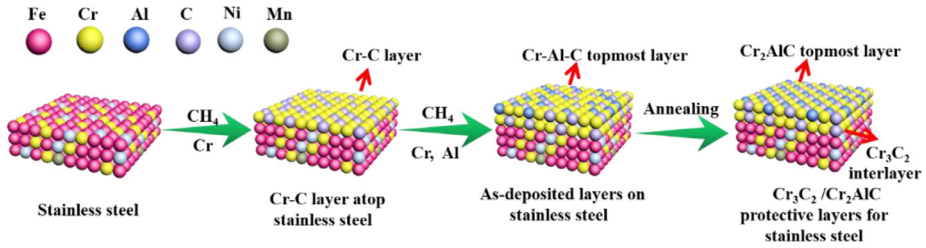

Fig. 1. Schematic illustration of Cr_2AlC layer deposited on SS316L substrate.

2.2. Characterization of material

The X-ray diffraction (XRD) measurements of the samples were characterized by the Bruker D8 Advanced diffractometer with Cu K_α radiation (λ =1.54056 Å). The chemical compositions of the coatings were characterized using XPS. The cross-sectional morphologies of the products were investigated by scanning electron microscopy (SEM). For the SEM measurements, a Quanta 250 FEG instrument was used, equipped with an Oxford energy-dispersive spectrometer (EDS), which operated at an accelerating voltage of 15 kV. The TEM and high-resolution transmission electron microscopy (HRTEM) analysis images were performed on a field emission transmission electron microscopy using a Talos F200 at the operating voltage of 200 keV. The scanning transmission electron microscopy (STEM) and EDS mapping of the products were performed at Talos F200 equipped with a high-angle annular dark field (HAADF) detector.

2.3. ICR and electrochemical measurements

The ICR of coated and uncoated SS316L under the compaction forces was charactered by following our previous reported method [6]. The ICR values before and after potentiostatic polarization in the simulated PEMFC environments were tested for comparison to study the influence of corrosion. For the ICR test, two pieces of conductive carbon paper (Toray TGP-H-060) were sandwiched between the samples and two gold coated copper plates. The test pressure about 1.5 MPa was offered by a microcomputer with a universal electronic testing machine. The external circuit was set at a constant current of 1 A, and a precision multimeter was used to measure the voltage change of the whole circuit. Finally, the interface conductive resistance in the circuit was calculated by voltammetry. Electrochemical corrosion measurements of BPs, including potentiodynamic and potentiostatic method tests were performed by the Gamry electrochemical workstation in a standard three-electrode system. The as-prepared uncoated SS316L and coated ones were used as the working electrodes, while a Pt plate and an Ag/AgCl electrode were used as the counter and reference electrode, respectively. Prior to the measurements, the samples were initially reduced potentiostatically at −1.5 V (vs. Ag/AgCl) for 2 min to remove air-formed oxides on the surface and then kept in solution until a stable corrosion potential was attained. Corrosion resistance activity was analyzed by potentiodynamic polarization with the potential ranging from −0.5 to 1.25 V (vs. Ag/AgCl) at a 0.5 mV s^{-1} sweep rate during the simulated PEMFCs environment (0.5 M H_2SO_4 + 5 ppm HF solution at 80 °C bubbled with the pressured oxygen). During the potentiostatic polarization, the working electrode potential was kept constant at 0.6 V (vs. Ag/AgCl) bubbled with oxygen for 12 h, in order to evaluate the corrosion stability of the Cr_2AlC protective layer. After the potentiostatic test, 100 mL solution was collected and analysed by inductively-coupled plasma optical emission spectroscopy (ICP-OES).

2.4. Contact angle measurements

Wettability property of the bipolar plate is very important in water management during real operation of the fuel cell, and can be directly determined by measuring the contact angle with water using a contact angle goniometer (Dataphysics OCA-20) at room temperature (25 °C). To avoid experimental errors three different areas were tested on each sample, and then the contact angle was calculated using a drop shape analyzer.

2.5. Computational details

The thickness of slab was set as 13 atomic layers for (002) plane and 8 atomic layers for (103) plane. A 15 Å vacuum layer was added along *z* axis to avoid interaction of adjacent slabs after convergence test. The constructed configurations were simulated using Vienna ab-initio simulation package (VASP) and the core-valence interaction was described by the projector-augmented wave (PAW) method [49,50]. The generalized gradient approximation (GGA) Perdew-Burke-Ernzerhof (PBE) exchange-correlation function was applied [51]. The dipole correction along *z* axis was implemented to correct the errors introduced by the periodic boundary conditions. The Brillouin zone integration with a 4 × 4 × 1 k-points grid for (002) model and a 2 × 6 × 1 k-points grid for (103) model was performed (Fig. S1, supporting information). The surface atoms were fully relaxed until the energy and force at every atom were respectively less than 1×10^{-4} eV $atom^{-1}$ and 0.05 eV $Å^{-1}$.

3. Results and discussion

The cross-sectional images and EDS line scanning of the Cr_2AlC layer with various deposited time of transition layer were shown in Fig. 2. The SEM images displayed that the prepared coatings were composed of inner Cr-C layer and outer Cr-Al-C layer, and the microstructures were homogenous and dense. From the EDS line scanning analyses (Fig. 2(a'-c')), it was showed that the thickness of the transition layer varies with the deposition time. As could be clearly seen that under the different deposited time (20, 40, 60 min), the thickness of transition layer was about 0.76 μm, 1.51 μm and 2.29 μm, respectively. Moreover, the cross-sectional morphologies and the corresponding EDS mapping of S20, S40 and S60 were also presented (Figs. S2-S4; supporting information). Combined with the EDS mapping results of the as-prepared coatings, it was obviously that Cr, Al and C were evenly distributed in the layer. Furthermore, the strong adherent interface between layer and substrate was clear and relatively sharp, without any defects such as columnar structure and cracks.

The XRD spectra were carried out to investigate the structure information of the coatings. As shown in Fig. 3(a), all peaks were ascribed to Cr_2AlC phase referring to the standard card PDF#29–0017. Obviously, with the increase of thickness of the transition layer, the peak intensity at (002) direction gradually decreased, and that at (103) direction became larger, that was to say the preferred orientation (103) of the Cr_2AlC crystal plane appeared.

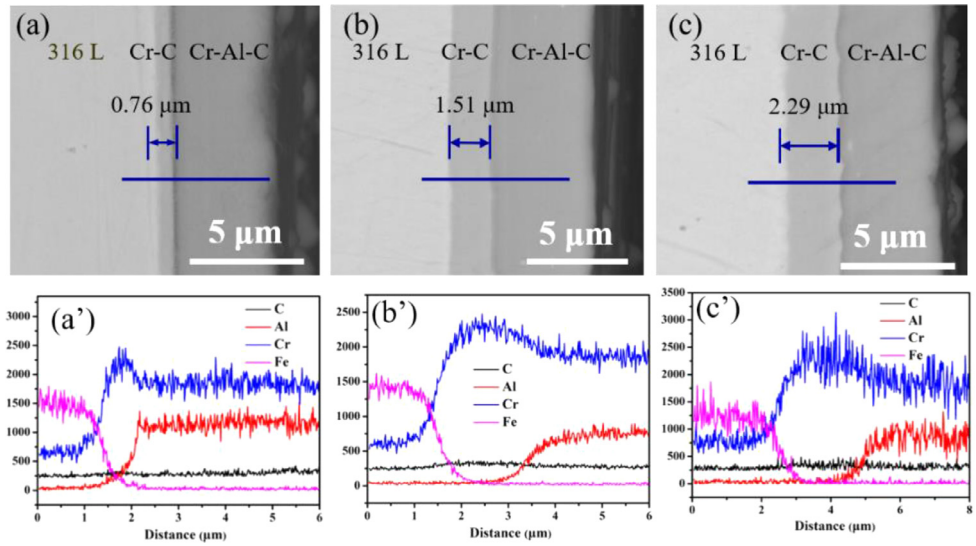

Fig. 2. Cross-sectional morphologies of the Cr_2AlC coatings with various deposited time of transition layer: (a) 20 min, (b) 40 min, (c) 60 min, and (a'-c') the corresponding EDS line-scanning.

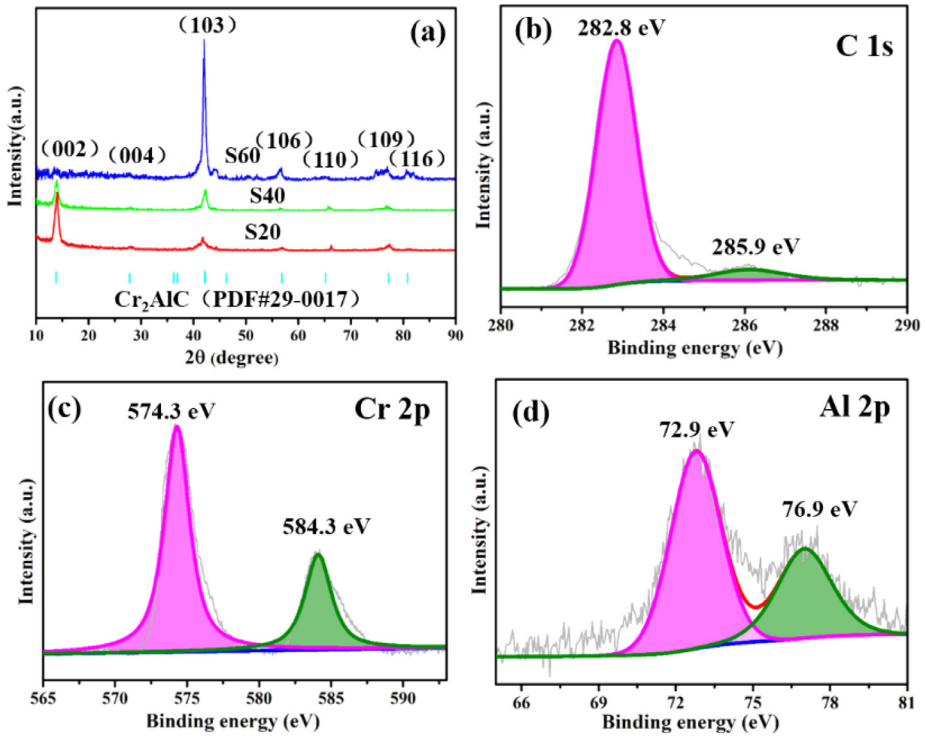

Fig. 3. (a) XRD and (b-d) XPS spectra of Cr_2AlC coatings deposited on SS316L substrate.

This phenomenon may be as a consequence of the competition between the strain energy and surface energy of the transition layer at different thickness, and thus affecting the growth of the topmost Cr_2AlC layer [52,53]. Simultaneously, the XRD patterns of SS316L and the sample that only Cr-C layer deposited with 60 min after standard heat treatment were also provided (Fig. S5, supporting information). The as-prepared sample only with Cr-C layer identified the crystalline phases as being Cr_3C_2 indexed by standard card PDF#35–0804, therefore, the composition of the transition layer was determined to be Cr_3C_2. For further investigate the composition of the coatings, the XPS measurement was performed (Fig. 3(b-d)). It was obviously that a typical carbide-like carbon and adsorbed carbon were demonstrated at the peaks of 282.8 eV and 285.9 eV, respectively [53,54]. In the spectrum of Cr 2p (Fig. 3(c)) the peak at 574.3 eV was assigned to $2p_{3/2}$, which was in line with the values reported for chromium carbide [55]. The peaks located at 72.9 eV and 76.9 eV in Fig. 3(d) formally corresponded to metallic aluminum [48,56]. Above all, it could be assumed that the Cr_2AlC layer with a hexagonal close packed crystal structure was formed.

Fig. 4 showed the TEM and HRTEM images of as-prepared Cr_2AlC coating. As reported in our previous studies [27], the coating exhibited dense crystal structure and along the growth direction the smaller of the grain size (Fig. 4(a)). The HRTEM images clearly showed that the spacing of adjacent lattice fringes was 0.641 nm, which matched well with the lattice constants of (002)

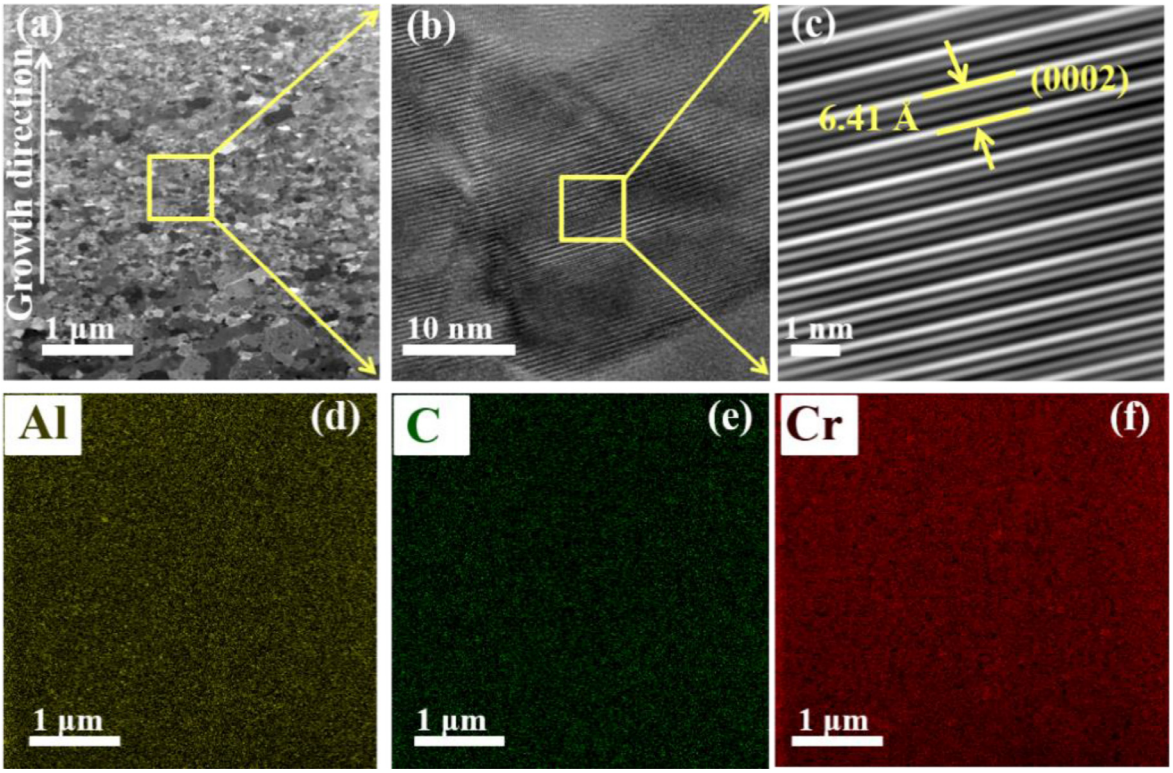

Fig. 4. TEM and HADDF-EDX mapping images of Cr_2AlC layer: (a) bright-field image, (b, c) HRTEM image, (d, e, f) HADDF-EDX element mapping of Al, C and Cr.

planes in Fig. 3(a). In order to further investigate the distribution of the Cr, Al and C components, the aberration corrected HAADF-EDX mapping was performed. The analysis results clearly revealed that the Cr, Al and C components distribute uniformly in the coatings. Hence, it was further concluded that the prepared coatings were Cr_2AlC MAX phase.

As we all know, corrosion resistance was one of the most important criterions in assessing the performance of BPs in PEMFCs environment [57]. The electrochemical corrosion resistance behaviors of coated specimen as well as bare SS316L were tested at 80 °C using 0.5 M H_2SO_4 + 5 ppm HF solution with oxygen bubbled. Fig. 5 presented the electrochemical behaviors of coated specimen as well as bare SS316L. The corrosion current densities (I_{corr}) and corrosion potentials (E_{corr}) of samples coated Cr_2AlC with varying thickness of transition layer were performed by the potentiodynamic polarization curves showed in Fig. 5(a). Obviously, the coated samples showed higher E_{corr} and lower I_{corr} compared with the bare SS316L substrate, and the detail values were summarized in supporting information (Table S3, supporting information). From the result, it could be concluded that all the coatings deposited on SS316Lsubstrates were available to improve the corrosion resistance. The sample S60 showed the best corrosion resistance, and the corrosion current density was lower than those of other samples. Its I_{corr} was 6.8×10^{-2} μA cm^{-2} at the applied voltage (0.6 V, which was much lower than the 2025 technical target ($< 10^{-6}$ A cm^{-2}) proposed by the US DOE [8]. Moreover, this was a marked low value compared with graphite BPs as reported in previous literatures (Table S4, supporting information). The highest levels of corrosion resistance obtained might be ascribed to the preferred (103) orientation as shown in Fig. 3(a). To obtain the further insight into the corrosion resistance of the coated SS316L under the simulated PEMFC environments, we provided the detail dissolution current density values at –0.0705 V and +0.6295 V (vs. Ag/AgCl) of potentiodynamic polarization in supporting information (Table S5, supporting information). Furthermore, for analog the normal loading process observed in simulated PEMFC environments, long-term durability tests of specimens were performed in order to simulate the normal loading process observed in simulated PEMFC environments. The current density curves of the as-prepared samples were illustrated in Fig. 5(b), and their final stable current densities were presented in Fig. 5(c). It was clearly seen that during the potentiostatic polarization test, the sample with transition layer deposited for 60 min presented the best corrosion resistance with an average current density of 9.0×10^{-3} μA cm^{-2}, which was much lower than that of bare SS316L. It was worth mentioning that all current density values of the samples coated Cr_2AlC layer could meet the requirement of DOE. Moreover, to verify the corrosion resistance of the Cr_3C_2 layer, the potentiodynamic and potentiostatic polarization curves of sample only with transition layer were also supplied (Fig. S6, supporting information). The current density was lower than that of the bare SS316L, but it was much higher than those of samples with Cr_2AlC layer. Therefore, the observation exhibited that the excellent corrosion resistance mainly dominated by outermost Cr_2AlC layer.

The ICR was another one of the most important properties under the PEMFC real working conditions, which would not only increase power consumption but also would reduce the output current of fuel cells. The ICR was mainly determined by the electrical conductivity of the contact surface and the real contact area [58]. In the section, the ICR tests before and after the long-time potentiostatic polarization of bare and coated SS316L were shown in Fig. 5(d). It was worth to mention that the ICR values of those samples possessed the lowest value of 3.16 mΩ cm^2, which was much lower than 80 mΩ cm^2 of bare SS316L, resulting from the good electrical conductivity of the outermost Cr_2AlC coatings. On the basis of the studies [31], the first-principle showed that MAX phase materials had high electronic density of states at Fermi level (E_f) and resulted in an excellent electrical conductivity. Actually, the E_f of Cr_2AlC located below the valence band maximum near the Γ point. The finite density of states of Cr_2AlC at E_f, $N(E_f)$ (to-

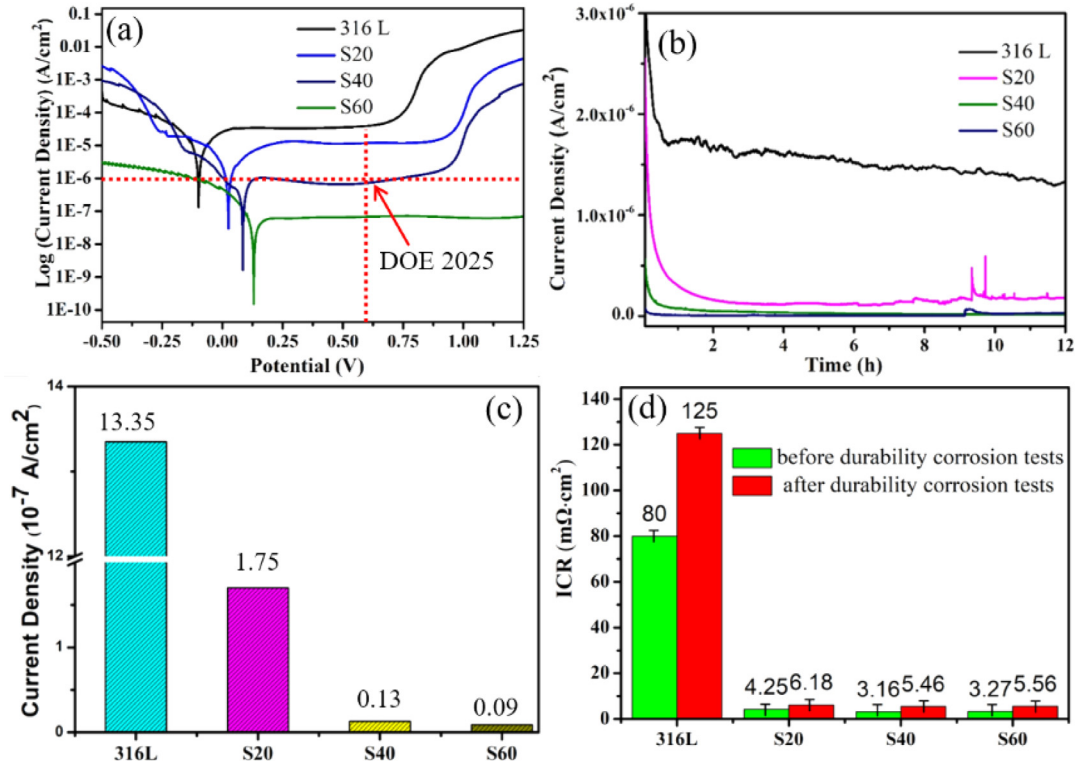

Fig. 5. (a) Potentiodynamic polarization curves observed in the acid corrosion electrolyte at 80 °C. (b) Long-time potentiostatic tests on bare and coated SS316L with 0.6 V vs. Ag/AgCl, in acid corrosion electrolyte at 80 °C for 12 h. (c) Corresponding final stable current densities. (d) The ICR values of the samples before and after the long-time potentiostatic tests.

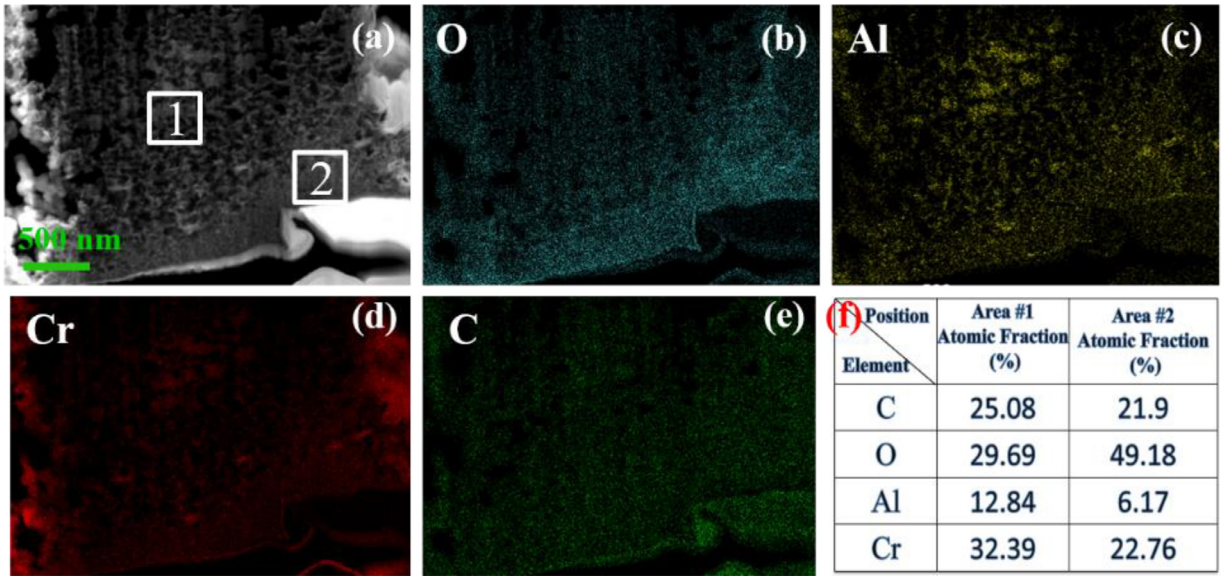

Position / Element	Area #1 Atomic Fraction (%)	Area #2 Atomic Fraction (%)
C	25.08	21.9
O	29.69	49.18
Al	12.84	6.17
Cr	32.39	22.76

Fig. 6. (a) HAADF images of the Cr_2AlC coating and (b-e) the corresponding EDS mapping, (f) element atomic fraction of area 1 and area 2 from (a) after the long-time potentiostatic test.

tal density of states at the Fermi level E_f) was 6.0 states eV^{-1} cell [59]. More interestingly, the ICR of all the coated SS316L samples increased a little after potentiostatic polarization for 12 h, which was better than previous work [60,61]. The minor increase in the ICR value could be attributed to the formed of the semiconductor passivation film during the potentiostatic polarization test. Above all, it indicated that the Cr_2AlC coatings could effectively reduce the ICR, and confer SS316L high durability of corrosion resistance.

The cross-sectional morphologies of S60 after the long-time potentiostatic measurement were analyzed using HAADF and corresponding EDS mapping (Fig. 6). It was obviously observed that the surface area 2 was rich in O element than that of inner area1, which suggested that after long-time potentiostatic test the passive films were formed at the surface of the sample. The TEM bright-field and HRTEM images were shown in Fig. 7(a-c). The HRTEM images clearly showed that the spacing of the adjacent lattice fringe was 0.2047 nm, which was consistent well with the lattice constants (202) of Cr_2O_3 [62]. Furthermore, XPS analyses were performed to study the chemical compositions of passivated surface after long-time potentiostatic polarization (Fig. 7(d-f)). It should be

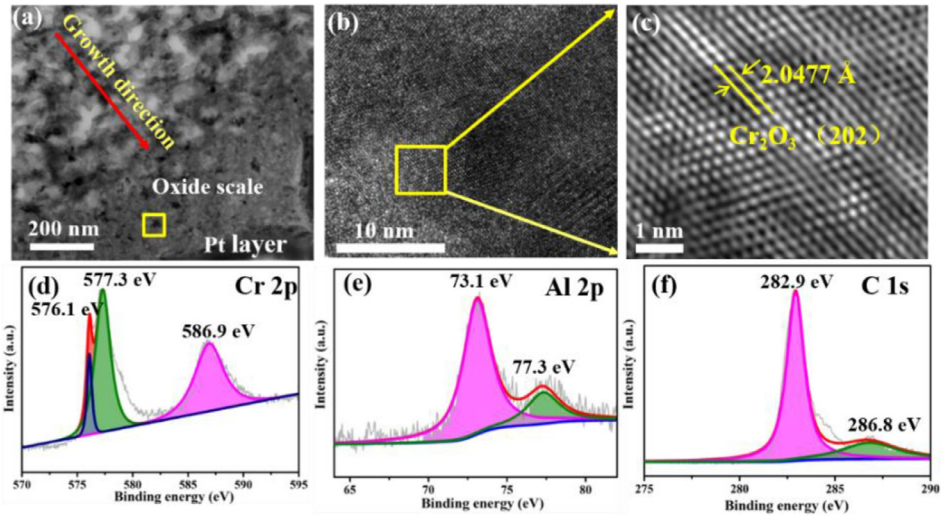

Fig. 7. (a) TEM bright-field image, (b, c) HRTEM image (d, e, f) XPS spectra of Cr_2AlC coating after the long-time potentiostatic test.

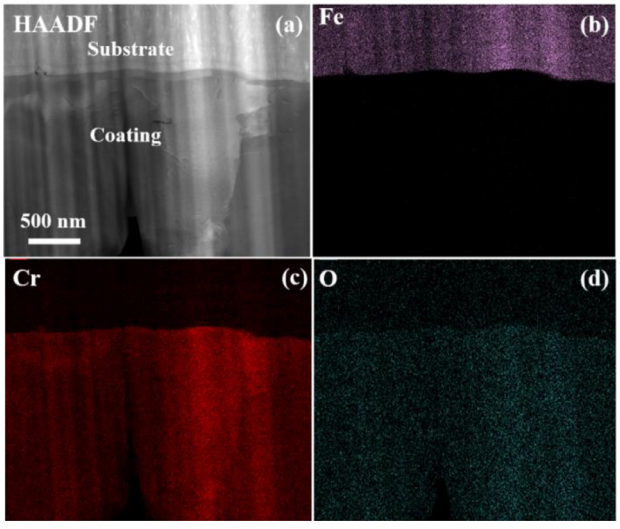

Fig. 8. TEM-HADDF and EDX mapping images between substrate and Cr_2AlC layer after the long-time potentiostatic test: (a) HADDF image, (b, c, d) HADDF-EDX element mapping of Fe, Cr and O.

pointed out that after the potentiostatic test some change taken place on the chemical environment of Cr element. The Cr 2p spectrum had three peaks at 576.1 eV, 577.3 eV and 586. 9 eV, which verified that Cr was in the form of the Cr^{3+} oxidation state [63,64]. The result confirmed that after the potentiostatic test the passive film Cr_2O_3 was formed on the surface of the Cr_2AlC layer, which was in accordance with previous reports [27]. While for the Al and C elements, there were shift relative to that before the potentiostatic test, which might be ascribed to the appearance of Cr_2O_3 resulting in the increase of Al-C bonds after the test [53].

Considering the interface corrosion occurred between substrate and coating layer was also another factor to increase the ICR, the TEM-HAADF characterization was further conducted between substrate and coatings layer after the long-time potentiostatic test. Fig. 8 shows the TEM-HADDF and EDX mapping images between substrate and coatings, where a continuous and well bonded interface emerged distinctly. The corresponding EDS scanning, shown in Fig. 8(b-d), also revealed the formed obvious interface and oxygen-rich area was invisible between the substrate and coatings layer. It could be concluded that the interface corrosion was not observed since the Fe atoms and Cr atoms were not missing at the interface.

Table 1
Concentrations of Fe and Cr ions leached from SS316L and coated under simulated PEMFC operational conditions after 12 h potentiostatic test.

Samples	Concentrations of Fe (ppm)	Concentrations of Cr (ppm)
Bare 316L	9.63	0.65
S20	0.019	10.515
S40	0.013	10.305
S60	0.015	10.005

Since the corrosion of the Cr_2AlC coatings, metallic ions would be released from BPs to the solution, which played the important role in assessing the performance of bipolar plate materials [65]. The solutions after the potentiostatic test for 12 h were collected and the dissolved metal ions were determined by ICP-OES. As illustrated in Table 1, the concentrations of Fe ions in the solution reached the maximum values at around 9.63 ppm for bare SS316L. However, it was significantly reduced about three orders to 0.013–0.019 ppm after the application of Cr_2AlC coatings. Noted that the concentration of Cr ions for coatings with various phase orientations were almost kept at 10.26±0.255 ppm, which was about 16 time higher than that of bare SS316L at 0.65 ppm. As a consequence, it could be said that the Cr_2AlC coatings with various phase orientation not only suppressed the release of Fe ions from SS316L substrate to the solution significantly, but also demonstrated the corrosion at the surface of the Cr_2AlC coatings.

In order to better understand why the samples coated Cr_2AlC layer with transition layer deposited for 60 min showed the best corrosion resistance, the density-functional calculations were performed in contact with oxygen adsorption. According to XRD patterns, with the increase of the thickness of the transition layer, the Cr_2AlC layer has a preferred orientation (103). The single O atom was initially placed on eight different sites: Top (T) and Bridge (B) sites of C, Top (T) and Bridge (B) sites of Al and Top (T), Bridge (B), FCC (F)- and HCP (H)-hollow sites of Cr at the surface of (103) model (Fig. 9(a)). The adsorption energy (E_{ads}) of these sites were calculated by:

$$E_{ads}=E_{slab/O}-E_{slab}-\frac{1}{2}E_{O_2}$$

where the $E_{slab/O}$, E_{slab} and E_{O_2} were the energy of adsorption models, clean slab and O_2 molecule in the gas, respectively. The E_{ads} of FCC-hollow (F) adsorption site for (002) model was also calculated, since it was the most negative at the surface of (002) plane [66]. The computational results demonstrated that the F site

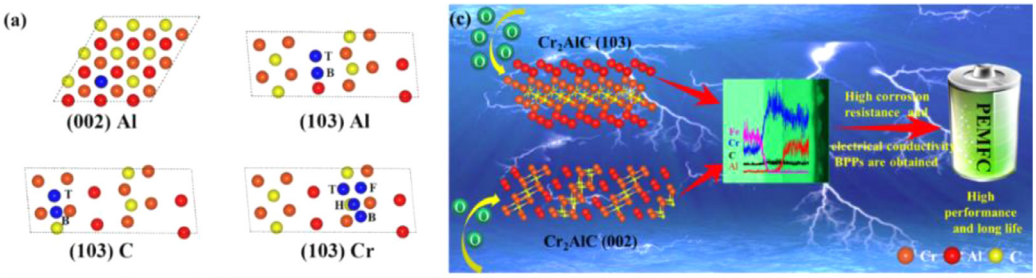

(b)

	(002)	(103)						
		Al-T	Al-B	C-T	C-B	Cr-T	Cr-B	Cr-H	Cr-F
E_{ads} (eV)	-4.68	-4.24	-3.67	-1.97	-3.74	-3.63	-4.71	-4.62	-4.82

Fig. 9. (a) Adsorption sites of O atom. (b) Adsorption energies of O atom absorbed on the surface of (002) and (103) planes at different adsorption sites. (c) Concise schematic diagrams mechanism showing the conductivity and corrosion resistance of Cr_2AlC.

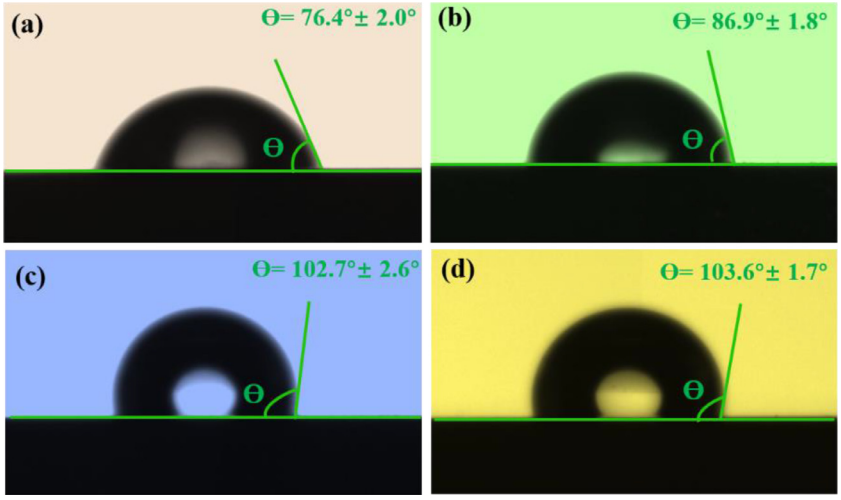

Fig. 10. Contact angles of (a) 316 L, (b) S20, (c) S40, and (d) S60 with water, respectively.

of Cr at the surface of (103) model exhibited the most negative E_{ads}, indicating that O atoms prefer to adsorb at this site (Fig. 9(b)). Based on the calculations results, it was easier to form oxide layer of the sample with (103) preferred orientation than that of (002), and a speculative mechanism was proposed to account for excellent corrosion resistance (Fig. 9(c)).

In addition, considering the PEMFCs are operated with water circumstances, the controlled surface wettability needs to be concerned for the bipolar plate during water management process [7]. In particular, if the generated liquid water caused by the oxygen reaction could not be removed in time, the water would prevent the reactant gasses from entering the electrode significantly in fuel cell stack, leading to the electrode flooding disaster with serving time [67]. As shown in Fig. 10, the contact angles of Cr_2AlC coating with various phase orientations were approximately 86.9°−103.6°, which were higher than that of SS316L at 76.4°±2°, implying the enhanced hydrophobicity after coating. This not only could avoid the water flooding in the cell stack, but also prevent the water adhering on the surface of SS316L substrate accelerating the corrosion of metal BPs with prolonged serving time.

4. Conclusions

In conclusion, we have successfully demonstrated the Cr_2AlC coatings with various preferred orientation by homemade combined cathodic arc/sputter deposition system, followed by annealing treatment. The lowest ICR of SS316L coated with the Cr_2AlC was only 3.16 mΩ cm^2 at 1.5 MPa, which was attributed to its high electronic density of states at E_f. In particular, the Cr_2AlC coatings with preferred (103) orientation exhibited the lowest I_{corr} value of 2×10^{-2} μA cm^{-2}. The underlying mechanism behind this intriguing phenomenon was attributed to the formed oxide layer at the surface of the sample, which was certificated by both experiments and density-functional calculations. Furthermore, the contact angles of the Cr_2AlC coating samples with water were higher than that of SS316L, implying the enhanced hydrophobicity for benefit of water management in PEMFCs. Thus, Cr_2AlC coatings coated on SS316L could provide a promising and cost-effective strategy for metallic BPs in harsh PEMFCs.

Acknowledgements

This work was financially supported by the National Science Found for Distinguished Young Scholars of China (No. 52025014), the National Science and Technology Major Project (No. 2017-VII-0012–0108), the National Science Foundation of China (Nos. 51901238 and 52101109), and the Natural Science Foundation of Ningbo (Nos. 202003N4350 and 202003N4025).

Supplementary materials

Supplementary material associated with this article can be found, in the online version, at doi:10.1016/j.jmst.2021.06.069.

References

[1] A.G. Olabi, T. Wilberforce, M.A. Abdelkareem, Energy 214 (2021) 118955.
[2] K. Feng, Z. Li, H. Sun, L. Yu, X. Cai, Y. Wu, P.K. Chu, J. Power Sources 222 (2013) 351–358.
[3] R. Taherian, J. Power Sources 265 (2014) 370–390.
[4] R. Haider, Y. Wen, Z.F. Ma, D.P. Wilkinson, L. Zhang, X. Yuan, S. Song, J. Zhang, Chem. Soc. Rev. 50 (2021) 1138–1187.
[5] Y. Wang, D.F.R. Diaz, K.S. Chen, Z. Wang, X.C. Adroher, Mater. Today 32 (2020) 178–203.
[6] H. Li, P. Guo, D. Zhang, L.L. Liu, Z.Y. Wang, G.S. Ma, Y. Xin, P.L. Ke, H. Saito, A.Y. Wang, J. Power Sources 469 (2020) 228269.
[7] Y. Fu, G. Lin, M. Hou, B. Wu, Z. Shao, B. Yi, Int. J. Hydrogen Energy 34 (2009) 405–409.
[8] Y. Song, C. Zhang, C.Y. Ling, M. Han, R.Y. Yong, D. Sun, J. Chen, Int. J. Hydrogen Energy 7 (2019) 1–16.
[9] C.Y. Bai, T.M. Wen, K.H. Hou, M.D. Ger, J. Power Sources 195 (2010) 779–786.
[10] H. Sun, K. Cooke, G. Eitzinger, P. Hamilton, B. Pollet, Thin Solid Films 528 (2013) 199–204.
[11] S. Joseph, J.C. McClure, P.J. Sebastian, J. Moreira, E. Valenzuela, J. Power Sources 177 (2008) 161–166.
[12] S.H. Wang, J. Peng, W.B. Lui, J. Power Sources 160 (2006) 485–489.
[13] V.V. Nikam, R.G. Reddy, J. Power Sources 152 (2005) 146–155.
[14] R.F. Silva, D. Franchi, A. Leone, L. Pilloni, A. Masci, A. Pozio, Electrochim. Acta 51 (2006) 3592–3598.
[15] N.F. Asri, T. Husaini, A.B. Sulong, E.H. Majlan, W.R.W. Daud, Int. J. Hydrogen Energy 42 (2017) 9135–9148.
[16] K. Zhang, S. Sharma, Chem. Eng. 5 (2016) 277–286.
[17] P.Y. Yi, L. Peng, L. Feng, P. Gan, X.M. Lai, J. Power Sources 195 (2010) 7061–7066.
[18] M. Li, S. Luo, C. Zeng, J. Shen, H. Lin, C.N. Cao, Corros. Sci. 46 (2004) 1369–1380.
[19] Y. Zhao, L. Wei, P.Y. Yi, L. Peng, Int. J. Hydrogen Energy 41 (2016) 1142–1150.
[20] M.H. Ding, H.S. Zhang, C. Zhang, X. Jin, Surf. Coat. Technol. 224 (2013) 34–41.
[21] S.H. Wang, J. Peng, W.B. Lui, J.S. Zhang, J. Power Sources 162 (2006) 486–491.
[22] Y. Wang, D.O. Northwood, J. Power Sources 175 (2008) 40–48.
[23] P.Y. Yi, W. Zhang, F. Bi, L. Peng, X.M. Lai, ACS Appl. Mater. Interfaces 10 (2018) 19087–19096.
[24] Z.Y. Wang, J. Sun, B.B. Xu, Y. Liu, P.L. Ke, A.Y. Wang, J. Eur. Ceram. Soc. 40 (2020) 197–201.
[25] Z.Y. Wang, W. Li, C. Wang, H. Wu, P.L. Ke, A.Y. Wang, Mater. Lett. 261 (2020) 127160.
[26] Z.Y. Wang, W. Li, Y. Liu, J. Shuai, P.L. Ke, A.Y. Wang, Appl. Surf. Sci. 502 (2020) 144130.
[27] Z.Y. Wang, G.S. Ma, L.L. Liu, L. Wang, P.L. Ke, Q. Xue, A.Y. Wang, Corros. Sci. 167 (2020) 14430.
[28] V.D. Jovic, B.M. Jovic, S. Gupta, T. El-Raghy, M.W. Barsoum, Corros. Sci. 48 (2006) 4274–4282.
[29] D. Li, Y. Liang, X. Liu, Y. Zhou, J. Eur. Ceram. Soc. 30 (2010) 3227–3234.
[30] A.M. Rana, M.H. Ahmad, F.F. Russul, Eng. Tech. J. 33 (2015) 845–854.
[31] J.L. Lu, N. Abbas, J. Tang, R. Hu, G.M. Zhu, Electrochem. Commun. 105 (2019) 106490.
[32] J.L. Lu, N. Abbas, J.N. Tang, J. Tang, G.M. Zhu, Corros. Sci. 158 (2019) 108106.
[33] R.M. Fernández-Domene, E. Blasco-Tamarit, D.M. García-García, J. García-Antón, Electrochim. Acta 95 (2013) 1–11.
[34] H. Xu, L. Wang, D. Sun, H. Yu, Appl. Surf. Sci. 351 (2015) 367–373.
[35] Y. Wang, X. Cheng, X. Li, Electrochem. Commun. 57 (2015) 56–60.
[36] J. Moon, H.Y. Ha, S.J. Park, T.H. Lee, J.H. Jang, C.H. Lee, H.N. Han, H.U. Hong, J. Alloys Compd. 775 (2019) 1136–1146.
[37] P. Brito, É. Schuller, J. Silva, T.R. Campos, C.R. Araújo, J.R. Carneiro, Corros. Sci. 126 (2017) 366–373.
[38] K. Hagihara, M. Okubo, M. Yamasaki, T. Nakano, Corros. Sci. 109 (2016) 68–85.
[39] W. Wang, A. Alfantazi, Appl. Surf. Sci. 335 (2015) 223–226.
[40] G.L. Song, R. Mishra, Z. Xu, Electrochem. Commun. 12 (2010) 1009–1012.
[41] N. Wang, Y. Mu, W. Xiong, J. Zhang, Q. Li, Z. Shi, Corros. Sci. 144 (2018) 107–126.
[42] X. Wang, J.A. Szpunar, L. Zhang, Appl. Surf. Sci. 327 (2015) 532–536.
[43] E.A.S.Y. Liu, E.V. Koroleva, P. Skeldon, G.E. Thompson, X. Zhou, K. Shimizu, H. Habazaki, Corros. Sci. 45 (2003) 789–797.
[44] A. Ma, L. Zhang, D. Engelberg, Q. Hu, S. Guan, Y. Zheng, Corros. Sci. 164 (2020) 108320.
[45] Y.Q. Yan, W.X. Zhi, Z.C. Yan, W.P. Jia, L.W. Zhen, Y.F. Zhu, Corros. Sci. 170 (2020) 108643.
[46] E. Martinez-Lombardia, Y. Gonzalez-Garcia, L. Lapeire, I. De Graeve, K. Verbeken, L. Kestens, J.M.C. Mol, H. Terryn, Electrochim. Acta 116 (2014) 89–96.
[47] W. Tian, P. Wang, G. Zhang, Y. Kan, Y. Li, D. Yan, Scr. Mater. 54 (2006) 841–846.
[48] E.I. Zamulaeva, E.A. Levashov, E.A. Skryleva, T.A. Sviridova, P.V. Kiryukhantsev-Korneev, Surf. Coat. Technol. 298 (2016) 15–23.
[49] G. Kresse, J. Hafner, Phys. Rev. B 48 (1993) 13115–13118.
[50] G. Kresse, J. Furthmuller, Phys. Rev. B 54 (1996) 11169–11186.
[51] K.B. John, P. Perdew, M. Ernzerhof, Phys. Rev. Lett. (1996) 3685–3688.
[52] M.R. Field, P. Carlsson, P. Eklund, J.G. Partridge, D.G. McCulloch, D.R. McKenzie, M.M.M. Bilek, Surf. Coat. Technol. 259 (2014) 746–750.
[53] A. Obrosov, R. Gulyaev, A. Zak, M. Ratzke, M. Naveed, W. Dudzinski, S. Weiss, Materials 10 (2017) 2–16.
[54] D.V. Shtansky, P.V. Kiryukhantsev-Korneev, A.N. Sheveyko, B.N. Mavrin, C. Rojas, A. Fernandez, E.A. Levashov, Surf. Coat. Technol. 203 (2009) 3595–3609.
[55] M. Detroye, F. Reniers, C. Buess-Herman, J. Vereecken, Appl. Sur. Sci. 144 (1999) 78–82.
[56] J.P.R. Hauert, Interface 292 (1993) 121–129.
[57] F. Bi, L. Peng, P.Y. Yi, X.M. Lai, J. Power Sources 314 (2016) 58–65.
[58] P.Y. Yi, D. Zhang, L. Peng, X.M. Lai, ACS Appl. Mater. Interfaces 10 (2018) 34561–34572.
[59] Y. Mo, P. Rulis, W.Y. Ching, Phys. Rev. B 86 (2012) 165122.
[60] S. Joseph, J. McClure, R. Chianelli, P. Pich, P. Sebastian, Int. J. Hydrogen Energy 30 (2005) 1339–1344.
[61] J. Wang, J. Sun, S. Li, Z. Wen, S. Ji, Int. J. Hydrogen Energy 37 (2012) 1140–1144.
[62] P. Jin, S. Nakao, S.X. Wang, L.M. Wang, Appl. Phys. Lett. 82 (2003) 1024–1026.
[63] M.M. Alam, A.M. Asiri, M.T. Uddin, M.A. Islam, M.M. Rahman, RSC Adv 8 (2018) 12562–12572.
[64] K. Ghanbari, F. Nejabati, Anal. Methods 12 (2020) 1650–1661.
[65] K. Feng, G. Wu, Z. Li, X. Cai, P.K. Chu, Int. J. Hydrogen Energy 36 (2011) 13032–13042.
[66] N. Li, R. Sakidja, W.Y. Ching, Appl. Surf. Sci. 315 (2014) 45–54.
[67] Y. Fu, M. Hou, G. Lin, J. Hou, Z. Shao, B. Yi, J. Power Sources 176 (2008) 282–286.